



Multifunctional g-C₃N₄/graphene oxide wrapped sponge monoliths as highly efficient adsorbent and photocatalyst

Ruiyang Zhang^{a,b}, Minzhi Ma^b, Qian Zhang^b, Fan Dong^c, Ying Zhou^{a,b,*}

^a State Key Laboratory of Oil and Gas Reservoir Geology and Exploitation, Southwest Petroleum University, Chengdu 610500, China

^b The Center of New Energy Materials and Technology, School of Materials Science and Engineering, Southwest Petroleum University, Chengdu 610500, China

^c Chongqing Key Laboratory of Catalysis and Functional Organic Molecules, College of Environment and Resource, Chongqing Technology and Business University, Chongqing, 400067, China

ARTICLE INFO

Keywords:

g-C₃N₄/graphene oxide
Melamine sponge
Photocatalysis
Environmental remediation
CO₂ reduction

ABSTRACT

Photocatalysis has been considered as a promising technology for environmental remediation and clean energy production. However, gas phase photocatalytic reaction suffers from the challenges of difficult dispersion and recovery. To overcome these weaknesses, we designed and successfully fabricated a new-type g-C₃N₄/graphene oxide (GO)-wrapped melamine sponge (MS) monolith. In this case, g-C₃N₄ photocatalyst is uniformly dispersed on the surface of GO, making full use of incident light and contacting with pollutant efficiently. GO acts as a bridge to connect the g-C₃N₄ and MS. Meanwhile, it can accelerate the separation of photogenerated electrons and holes. Moreover, MS maintains its excellent elasticity and recoverability avoiding the intricate operation in the recycling procedure, and possesses abundant porous structure contributing to the efficient transportation of gas molecules into the reaction sites. As a proof of concept, the obtained g-C₃N₄/GO-wrapped sponge reveals favorable adsorption capacity for both dyes and organic solvents and achieves a max NO removal ratio of 45.9% as well as high CO, CH₄ and H₂ evolution of 42.9, 4.6 and 1.6 μmol g⁻¹ h⁻¹, which is 2.9-, 6.4- and 27.1-folds enhancement over g-C₃N₄/GO composite. This work provides fresh insights into the development of efficient monolithic photocatalyst for a wide range of applications.

1. Introduction

In decades, with the rapid development of industry and the extensive utilization of fossil fuels, environmental pollution and depletion of global energy resources have become one of the most crisis issues that are significantly threatening the development of human society [1–3]. Since Fujishima and Honda reported the photocatalytic hydrogen evolution over TiO₂ electrode in 1972 [4], photocatalysis has been considered as a promising green technology which meets the demand of environmental remediation and clean energy production [5–8]. Among the reported photocatalysts, graphitic carbon nitride (g-C₃N₄) as a metal-free and visible-light-responsive photocatalyst has attracted wide attention around the world [9,10]. Tunable electronic band structure, favorable physical and chemical stability and facile synthesis route make g-C₃N₄ possess great potential application in hydrogen evolution, environmental remediation, CO₂ reduction, and so on [9,11–14]. Nevertheless, the photocatalytic performance of g-C₃N₄ is significantly limited by its inherent deficiency including low surface area, rapid recombination rate of photogenerated electron-hole pairs and inefficient utilization of light energy. Therefore, various strategies

have been proposed to overcome aforementioned problems such as physical/chemical exfoliation [15,16], metal/non-metal doping [17–21], fabrication of heterojunctions [11,22–33], and so on. However, most of the efforts only focus on the catalyst itself, while this powder g-C₃N₄ suffers from great challenges in the gas phase photocatalytic process. One is the difficult dispersion. It is well known that favorable dispersibility can increase not only the light absorption but also the contact area between pollutant and photocatalyst which significantly affects the photocatalytic reaction. Powdery photocatalyst usually has a strong tendency to agglomerate. Therefore, the gas only flows on the surface of photocatalyst at the top of reactor and most of the photocatalyst can hardly absorb light and contact with the gas owing to the block of agglomeration. Another one is the intricate operations for recovering. Powdery photocatalyst can be blow off by airflow increasing the difficulty of recycling. Furthermore, the powder may enter into the gas circuit, leading to the damage of detector. Hence, some powders will be lost after the gas reaction owing to the airflow [34].

To overcome these weaknesses, three dimensional (3D) graphene aerogel (GA) and its derivatives (reduced graphene oxide (RGO) aerogel

* Corresponding author at: State Key Laboratory of Oil and Gas Reservoir Geology and Exploitation, Southwest Petroleum University, Chengdu 610500, China.
E-mail address: yzhou@swpu.edu.cn (Y. Zhou).

and graphene oxide (GO) aerogel) with large surface area, low density and high porosity are particularly attractive [35]. In this case, powdery photocatalyst can be uniformly loaded on the surface of framework of GA owing to its large surface area and high porosity, which make full use of light energy and contact with pollutant effectively. Furthermore, the monolithic body of GA makes it easy to recycle in both liquid and gas phase reactions and the porous structure provides facile transport pathway, allowing the reaction molecular to transfer to the active sites. More importantly, GA has a positive effect on photocatalytic performance which is attributed to its black body property and high conductivity [35–39]. Therefore, a 2D-2D g-C₃N₄/graphene macroscopic aerogel photocatalysts can be achieved with enhanced photocatalytic performance [40]. Unfortunately, the monolithic body of GA is usually fragile, which irreversibly disintegrate into debris or small block with micron size once in contact with a liquid or airflow [41,42]. As a result, all the benefits of GA will be lost in different degree including high porosity, the interface interaction between photocatalyst and GA, multidimensional electron transport pathway and the easy recoverability [41]. Recently, commercialized melamine sponge (MS) with extremely high elasticity and low cost shows great potential in environmental remediation [43,44]. Impressively, a synergistic effect can be achieved after the formation of graphene-wrapped sponge, in which MS as the framework maintains the high elasticity and reduce the cost while the cover of graphene endows it high conductivity to enhance photocatalytic performance [43,45]. Moreover, the porous structure of MS makes pollutants easy to transfer to the active sites. Therefore, graphene-wrapped sponge is a favorable alternative of pure GA. Nevertheless, to our best knowledge, architectural design of g-C₃N₄ coupling with graphene-wrapped sponge for environmental remediation and clean energy production represents a much less studied.

Inspired by considerations above, we designed a new-type g-C₃N₄/GO-wrapped sponge monolith prepared through a facile dipping-squeezing method followed by frozen-drying. In this system, g-C₃N₄ as the photocatalyst is uniformly dispersed on the surface of graphene nanosheets, enhancing the light absorption and increasing the contact area with pollutant. GO connects g-C₃N₄ and MS as a bridge and its high conductivity accelerates photogenerated electrons to transfer from g-C₃N₄ to GO, increasing the separation of electrons and holes. Furthermore, the strong mechanical property of sponge endows it with effective recoverability while its abundant porous structure provides efficient transport pathway for gas molecules to transfer to the catalytic sites. Impressively, g-C₃N₄/GO-wrapped sponge shows excellent adsorption capacity towards both dyes and organic solvents and enhanced photocatalytic performance for the oxidation of NO and reduction of CO₂, indicating its great potential in environmental remediation and clean energy production.

2. Experiments

2.1. Materials

All the chemicals were analytical grade reagents without any further purification before the experiment. Graphite powder (ca. 500 μm) was purchased from Qingdao Jin Ri Lai Graphite Co., Ltd. Urea was purchased from Tianjin Kemiou Chemical Co., Ltd. All other reagents were purchased from Chengdu Kelong Chemical Co., Ltd.

2.2. Synthesis of g-C₃N₄/GO suspension

The g-C₃N₄ powder was prepared by a thermal polymerization method. Typically, urea powders (15 g) are placed into a 100 mL alumina crucible with a cover. Then the crucible is heated to 550 °C at a heating rate of about 52 °C min⁻¹ in a muffle furnace for 1 h. Finally, the crucible is cooled naturally to room temperature and g-C₃N₄ powders with canary yellow color are obtained. The GO solution was prepared according to our previous work [35]. The g-C₃N₄/GO suspension

was synthesized as follow: Firstly, different amount of g-C₃N₄ powders (with the g-C₃N₄ and GO weight ratio of 0:1, 1:1, 3:1, 5:1, 7:1, 9:1) was added into 100 mL GO solution (1 mg mL⁻¹) and then the suspension was sonicated for 10 min and stirred until the suspension become uniform.

2.3. Synthesis of g-C₃N₄/GO-wrapped sponge

Firstly, the MS was immersed in 100 mL g-C₃N₄/GO suspension for 10 min and then the redundant g-C₃N₄/GO suspension on the surface of MS was removed through squeezing. Finally, the MS was frozen-drying for 48 h to remove water and the g-C₃N₄/GO-wrapped MS was achieved and marked as g-C₃N₄/GO-wrapped sponge. Unless otherwise stated, the g-C₃N₄/GO-wrapped sponge all refers to the weight ratio of g-C₃N₄ and GO with 7:1 in this work. For comparison, g-C₃N₄/GO (7:1) composite was prepared through direct frozen-drying of g-C₃N₄/GO suspension.

2.4. Characterization

Powder X-ray diffraction (XRD) analysis was performed by a PANalytical X'pert diffractometer operated at 40 kV and 40 mA using Cu Kα radiation. The morphology and microstructure of the as-prepared samples were observed by scanning electron microscope (SEM) using a ZEISS MERLIN Compact microscope and transmission electron microscope (TEM) was investigated on an FEI tecnai G2 F30 microscope. X-ray photoelectron spectroscopy (XPS) was carried out using a Thermo Scientific Escalab 250Xi spectrometer and Fourier transform infrared (FTIR) spectrum was recorded on a Thermo Nicolet 6700 spectrometer. UV–vis spectroscopy was measured on a Shimadzu UV-2600 spectrophotometer. Electron spin resonance (ESR) spectroscopy was performed on a Bruker E500 spectrometer. Photoluminescence (PL) measurements were recorded on a Hitachi F-7000 fluorescence spectrometer. The compressive test was performed on an MTS CMT4304 electro-mechanical universal testing machine.

2.5. Photocatalytic activity measurement

Photocatalytic NO oxidation was verified on a NO_x photocatalytic oxidation reactor reported in our previous work [35]. Typically, the samples with a diameter of 12 cm and a thickness of 0.5 cm were placed in the reactor using a 150 W metal halide lamp as a light source with or without a visible light filter (> 420 nm). A NO_x analyzer (Thermo Scientific, 42i-TL) was used to evaluate the concentration of NO and NO_x (including both NO and NO₂) during the photocatalytic reaction process.

Photoreduction of CO₂ was performed in a reactor with a volume of 380 mL. In a typical process, a plastic beaker with 20 mL deionized water in it was put in the reactor and then 100 mg sample dispersed in a glass culture dish was placed on the plastic beaker. Next, the reactor was first vacuumed by a pump and then Ar gas was injected into the reactor to remove air. Then 1 mL CO₂ was injected into the reactor. Finally, the reactor was placed on a stirrer under UV–vis illumination using a 300 W Xe lamp as a light resource. The amount of generated gas was analyzed with a Techcomp GC7900 gas chromatograph (GC). The GC contains a flame ionization detector (FID) and a thermal conductivity detector (TCD). CO and CH₄ were analyzed by the FID while H₂ were analyzed by the TCD.

Photodegradation of methyl orange (MO) over g-C₃N₄/GO-wrapped MS was performed through a reactor with a volume of about 200 mL. Typically, 50 mg samples were dispersed in the reactor with 100 mL MO solution (10 mg L⁻¹). After the adsorption-desorption equilibrium, the solution was illuminated using a 300 W Xe lamp as a light resource. The concentration of MO solution was measured using UV–vis spectroscopy (UV-5100, Anhui Wanyi). The effects of various radical scavengers on the degradation of MO were also examined to investigate the

underlying photodegradation mechanism. Isopropanol (IPA), benzoquinone (BQ) and methanol were introduced as the scavenger of $\cdot\text{OH}$, $\cdot\text{O}_2^-$ and h^+ , respectively.

2.6. Adsorption capacity and specific surface area measurement

To measure the adsorption capacity of organic solvent, 20 mg sample was added into different density organic solvents (tetrahydrofuran (THF), n-hexane, isopropanol, pyridine, carbon tetrachloride (CCl_4), dimethyl sulfoxide, xylene, ethanediol). After the adsorption-desorption equilibrium, the sample was weighed again. The adsorption capacity (Q_{wt}) was calculated using the following Eq. (1):

$$Q_{\text{wt}} = (m - m_0)/m_0 \quad (1)$$

where m_0 and m was the initial and equilibrium mass of the sample.

The adsorption capacity of dyes was performed as follow: Firstly, 40 mg sample was added into 200 mL dyes solution (20 mg L^{-1}); After reaching the adsorption-desorption equilibrium, the solution was measured using UV-vis spectroscopy (UV-5100, Anhui Wanyi) and the adsorption capacity (Q_e) was calculated using the following Eq. (2):

$$Q_e = (C_0 - C_e)V/m_s \quad (2)$$

where C_0 and C_e are the beginning and final concentrations of dyes, V is the volume of the dyes solution, and m_s is the mass of the sample, respectively.

The specific surface area (SSA) was measured through the methylene blue (MB) staining method and calculated using the following Eq. (3):

$$\text{SSA} = N_A \cdot A_{\text{MB}}(C_0 - C_e)V/(M_{\text{MB}} \cdot m_s) \quad (3)$$

where N_A is Avogadro's number ($6.02 \times 10^{23} \text{ mol}^{-1}$), A_{MB} is the surface coverage per molecule of MB (usually 1.35 nm^2), C_0 and C_e are the initial and equilibrium concentrations of MB, V is the volume of the MB solution, M_{MB} is the molecular mass of MB, and m_s is the mass of the sample, respectively.

3. Results and discussion

3.1. Fabrication of g-C₃N₄/GO-wrapped sponge

The preparation schematic of g-C₃N₄/GO-wrapped sponge was illustrated in Scheme 1A. Firstly, g-C₃N₄ powder was added in the GO solution. It is worth noting that owing to the lack of hydrophilic functional groups, the g-C₃N₄ powder was hardly dispersed in water leading to a layered suspension (Fig. S1), which makes it difficult to be equally loaded on sponge. After added it into GO solution, g-C₃N₄ powders were uniformly attached to the surface of GO nanosheets through the connection with the abundant oxygenic groups of GO, resulting in a uniform brown suspension. Secondly, the sponge was dipped in the suspension and then was squeezed to remove the excess solution. Finally, the additional water was removed through frozen-drying to form g-C₃N₄/GO-wrapped sponge monoliths. In comparison to g-C₃N₄/RGOA prepared through hydrothermal method [46], the g-C₃N₄/GO-wrapped sponge possesses low density ($6.8\text{--}11.7 \text{ mg cm}^{-3}$) depending on the loaded amount of g-C₃N₄ which make it stand on the ginkgo leaf, and can be simply cut into various shapes to meet different demands in the practical applications (Scheme 1B).

3.2. Structure, morphology, and optical properties of g-C₃N₄/GO-wrapped sponge

Fig. 1 shows the XRD patterns of g-C₃N₄/GO-wrapped sponge, GO-wrapped sponge, MS and g-C₃N₄ powder. Two peaks at 13.0° and 27.5° of g-C₃N₄ indicate the (100) and (002) reflections, while MS has two broad peaks at 10.8° and 22.9° assigned to two kinds of orientations of

MS chains [35,47]. After the introduction of GO, the peak at 10.8° become sharper and the intensity also increased, which is due to the cover of GO diffraction peak with the similar position. Moreover, a new diffraction peak at 27.5° corresponding to the (002) reflections of g-C₃N₄ can be observed after the formation of g-C₃N₄/GO-wrapped sponge, indicating the successful introduction of g-C₃N₄.

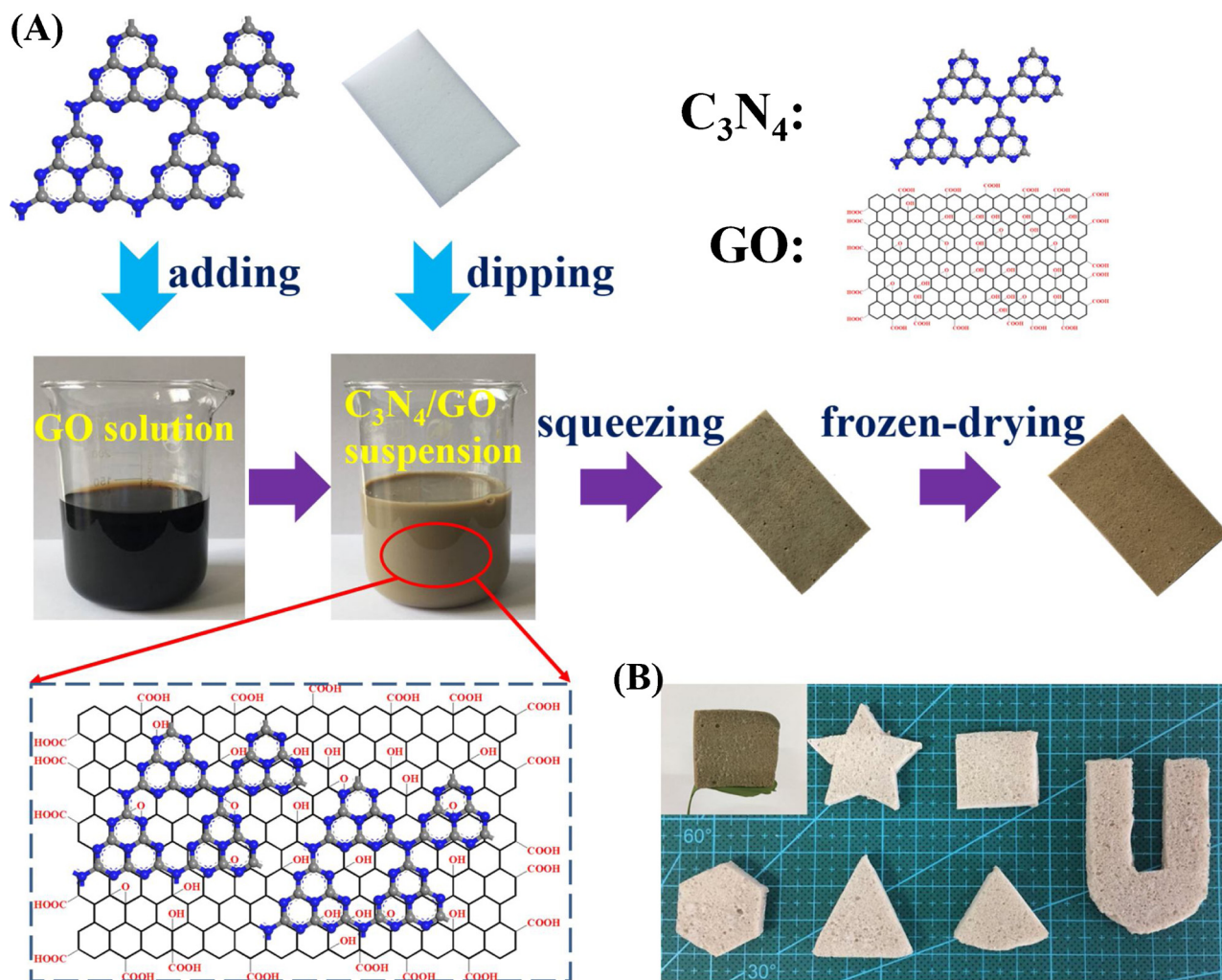
Morphology of MS and g-C₃N₄/GO-wrapped sponge was investigated through SEM. Close observation reveals that the surface of MS skeletons is relatively smooth, while after the formation of g-C₃N₄/GO-wrapped sponge, it is clearly observed that g-C₃N₄/GO composite was attached to the surface of MS (Fig. 2A and B). Fig. 2C shows the TEM of g-C₃N₄/GO-wrapped sponge. g-C₃N₄ nanosheets are dispersed on the surface of GO nanosheets. It is interesting that the g-C₃N₄ possesses abundant porous structure, which is caused by the ammonia gas generated during the pyrolysis process of urea [48]. Fig. S2 shows the HRTEM image of g-C₃N₄/GO-wrapped MS. Various dislocations and distortions of g-C₃N₄ can be observed owing to the low degree of crystallinity and the generated ammonia gas.

To verify the surface chemical composition of g-C₃N₄/GO-wrapped sponge, FTIR spectra studies were performed as shown in Fig. 3A. It has found that three bands of MS at 1622 , 1395 , 1084 cm^{-1} represent to C=N, C-N and C-O bonds while the band at 808 cm^{-1} is assigned to the triazine ring [49]. Several bands of g-C₃N₄ at $1249\text{--}1635 \text{ cm}^{-1}$ are assigned to the CN heterocycles which become broad after the fabrication of g-C₃N₄/GO-wrapped MS owing to the formation of hydrogen bonds between g-C₃N₄ and GO, while the band at 810 cm^{-1} corresponds to the triazine ring of g-C₃N₄ [35]. Importantly, the band at 3413 cm^{-1} represented to the -OH bond of MS is shifted to 3343 cm^{-1} and meanwhile becomes broad after the fabrication of g-C₃N₄/GO-wrapped sponge, confirming the interaction between g-C₃N₄/GO hybrid and MS through the formation of hydrogen bonds [37]. Fig. S3 shows the XPS of g-C₃N₄/GO-wrapped sponge. After calibrating the binding energy of the C 1s peak at 284.8 eV , the peak at 284.8 eV is ascribed to the sp^2 C-C bond while the peaks at 286.8 eV and 288.2 eV are assigned to the N-C=N and C-(N)₃ bonds. Correspondingly, the N 1s peaks at 398.7 eV and 400.1 eV are ascribed to C=N-C and N-(C)₃ bonds, respectively [50]. Moreover, the O 1s peak at 532.8 eV is assigned to the C-O bond, representing to the surface oxygen functional groups of GO [51]. These results demonstrate the strong interaction between g-C₃N₄/GO hybrid and MS.

Fig. 3B shows the UV-vis absorption spectra of these samples. The MS has two absorption peaks at 210 and 255 nm and an absorption edge around 278 nm while g-C₃N₄ powder with the main absorption peak at 361 nm has an absorption edge around 413 nm representing a bandgap of 3.00 eV . A strong light absorbance over the range of $200\text{--}700 \text{ nm}$ is observed for GO-wrapped sponge attributing to the surface sensitization of GO [52]. After the introduction of g-C₃N₄, the g-C₃N₄/GO-wrapped sponge reveals an enhanced visible-light absorption over the range of $400\text{--}650 \text{ nm}$ and a decreased bandgap of 2.89 eV compared with pristine g-C₃N₄ powder, which is attributed to the surface sensitization and black-body property of GO and is favor of photocatalytic performance.

3.3. Adsorption capacity of g-C₃N₄/GO-wrapped sponge

Dyes and organic solvents discharged from the industrial manufacture and household waste are the main sources of water pollution, which seriously destroys the ecological environment and threatens human health [53–55]. The as-prepared g-C₃N₄/GO-wrapped sponge shows excellent adsorption capacity towards both dyes and organic solvents. Fig. 4A presents the adsorption capacity of methylene blue (MB) and rhodamine B (RhB). The g-C₃N₄/GO-wrapped sponge possesses the highest adsorption capacity for MB (69.7 mg g^{-1}) and RhB (10.7 mg g^{-1}) which is higher than the sum of g-C₃N₄ powder (5.5 and 1.6 mg g^{-1}) and GO-wrapped sponge (47.8 and 5.1 mg g^{-1}), indicating the synergistic effect of GO and MS. In detail, g-C₃N₄ in powder form



Scheme 1. A): Schematic illustration of the preparation of g- C_3N_4 /GO-wrapped sponge; B): Image of different shapes of g- C_3N_4 /GO-wrapped sponge (inset: stand on the ginkgo leaf).

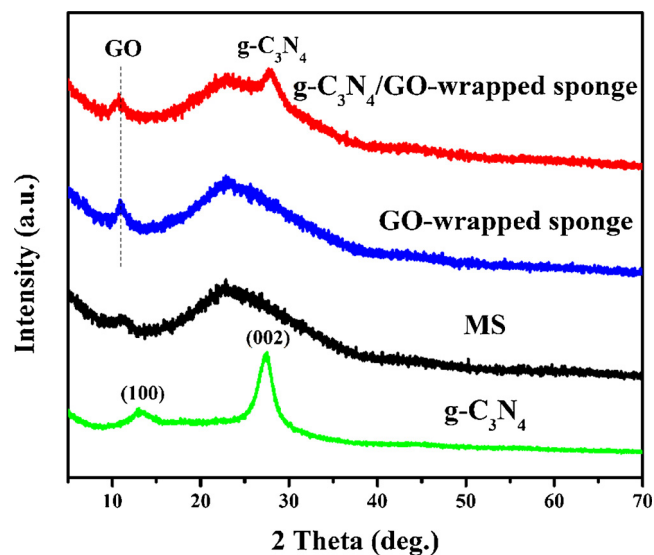


Fig. 1. XRD patterns of g- C_3N_4 , MS, GO-wrapped sponge and g- C_3N_4 /GO-wrapped sponge.

has a strong tendency to agglomerate which can block the porous structure, resulting in a low surface area ($14.0 \text{ m}^2 \text{ g}^{-1}$) and further leading to a low adsorption capacity. After added into GO solution, g- C_3N_4 are uniformly attached to the surface of graphene nanosheets, which avoid the block of the porous structure caused by agglomeration and the introduction of MS further disperses the g- C_3N_4 /GO composite, resulting in an enlarged surface area of $177.0 \text{ m}^2 \text{ g}^{-1}$. In addition, the porous structure of MS enables the pollutant to be efficiently adsorbed by g- C_3N_4 and GO. The synergistic effect of GO and MS significantly enhanced the adsorption capacity of g- C_3N_4 /GO-wrapped sponge. Fig. 4B illustrates adsorption capacities of $49.8\text{--}133.4 \text{ g g}^{-1}$ towards different organic solvent by g- C_3N_4 /GO-wrapped sponge, depending on their densities.

Impressively, the obtained g- C_3N_4 /GO-wrapped sponge maintains the mechanical property of original MS as shown in Fig. 5A and Fig. S4. After 100 cycles, the compressive strength of g- C_3N_4 /GO-wrapped sponge (5.08 kPa) still holds 63% of that of beginning (8.07 kPa). Although the compressed g- C_3N_4 /GO-wrapped sponge cannot completely recover to the original size, it can be applied in wastewater treatment already. Fig. 5B reveals the adsorption-squeezing process of g- C_3N_4 /GO-wrapped sponge. When g- C_3N_4 /GO-wrapped sponge was inserted into the glass dish, the *n*-hexane (stained with Sudan red) was adsorbed completely within 10 s and then the sample was taken out using a tweezer and squeezed to collect the *n*-hexane followed by further adsorption in a fresh system without any pretreatment. In short, these

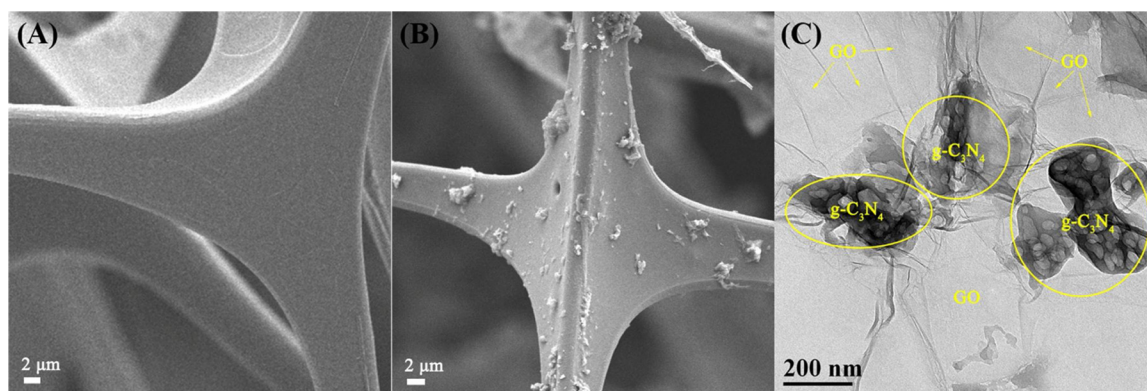


Fig. 2. SEM image of MS (A) and $g\text{-C}_3\text{N}_4/\text{GO}$ -wrapped sponge (B); C): TEM image of $g\text{-C}_3\text{N}_4/\text{GO}$ -wrapped sponge.

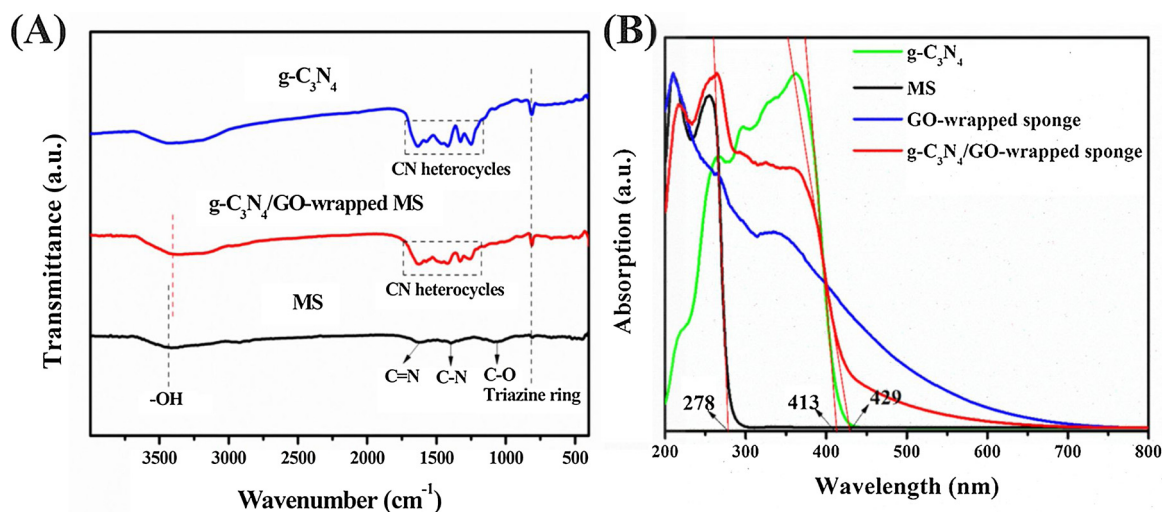


Fig. 3. FTIR (A) and UV-vis (B) spectra of different samples.

results indicate that the $g\text{-C}_3\text{N}_4/\text{GO}$ -wrapped sponge with favorable adsorption capacity and recyclability can be applied in wastewater treatment.

3.4. Photocatalytic performance of $g\text{-C}_3\text{N}_4/\text{GO}$ -wrapped sponge

The as-prepared $g\text{-C}_3\text{N}_4/\text{GO}$ -wrapped sponge possesses abundant porous structure and large surface area, which is significantly contributing to the efficient transportation of gas molecules into catalytic reaction sites, revealing its great potential for gas phase reaction

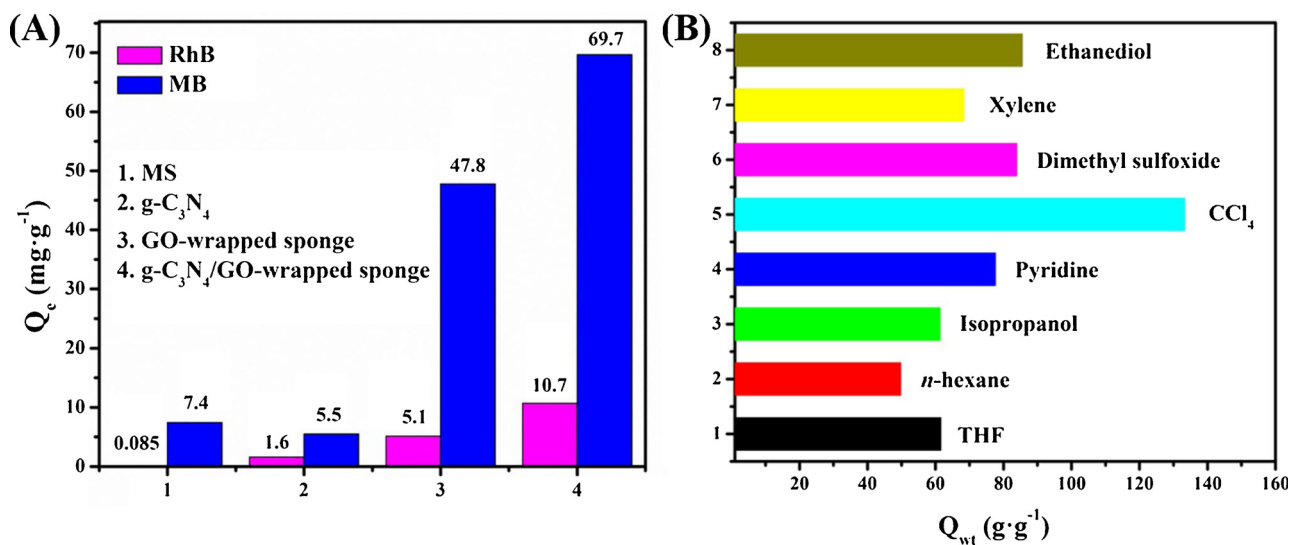


Fig. 4. Adsorption capacity towards different dyes (A) and organic solvents (B).

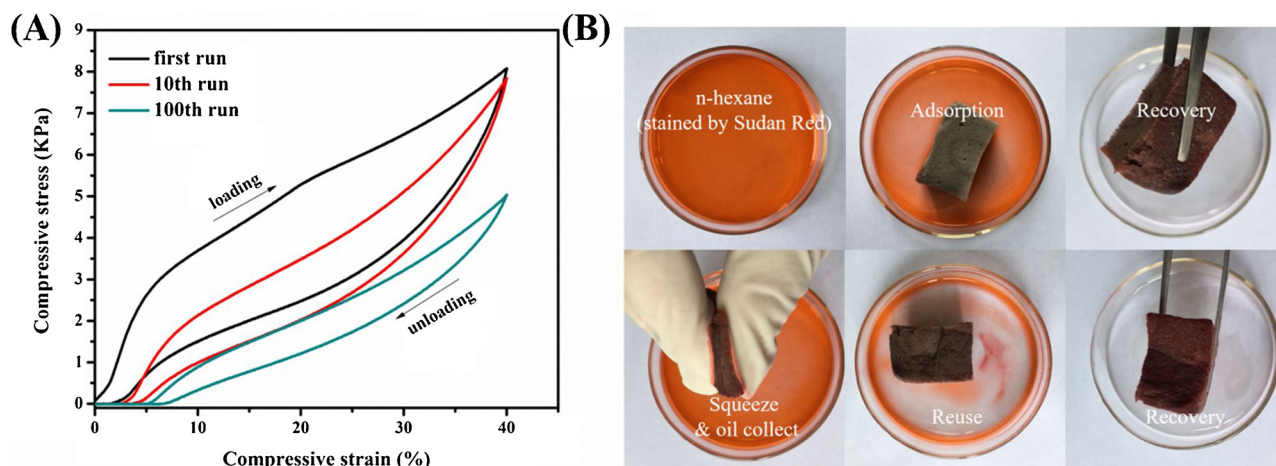


Fig. 5. A): Compressive stress-strain curves of g-C₃N₄/GO-wrapped sponge; B): Images of simple recovery of g-C₃N₄/GO-wrapped sponge through a tweezer and reuse.

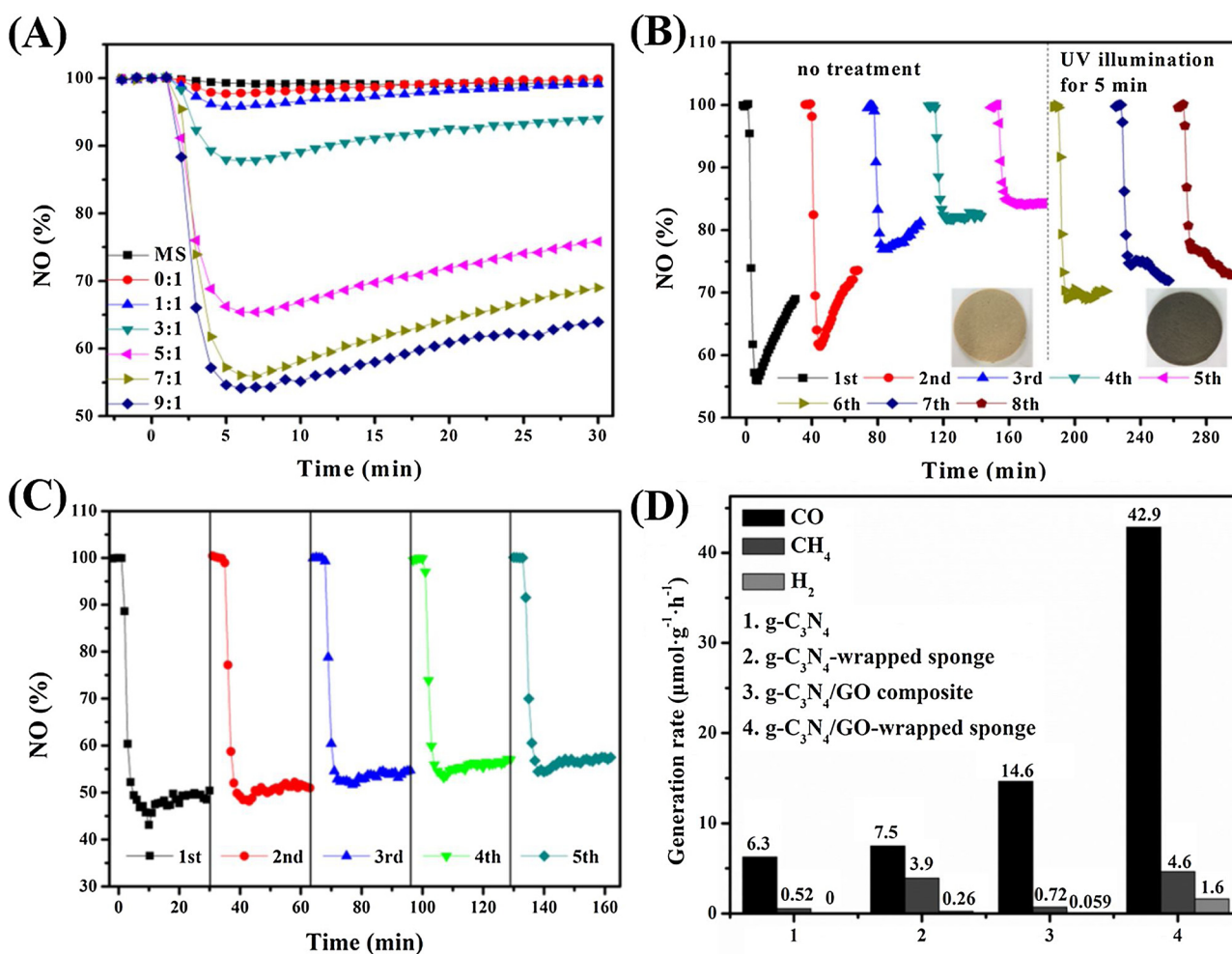


Fig. 6. A): Photocatalytic NO removal ratio; Photocatalytic recycle experiment on g-C₃N₄/GO-wrapped sponge (7:1) under visible light (B) and UV-vis light (C); D): Photoreduction of CO₂ under UV-vis light.

[41,56]. It should be noted that the g-C₃N₄/GO-wrapped sponge can be directly put into the reactor through cutting into various shapes to meet the different size demands of various reactors (Fig. S5A). Besides, the monolithic structure and the strong connection between g-C₃N₄/GO and MS make it hard to enter into reaction gas channel to destroy the reaction systems and easy to recycle compared to powder photocatalyst and the relatively thin thickness results in a favorable light absorption

(Fig. S5B). Moreover, the wrapped GO can protect MS from oxidation. Therefore, photocatalytic oxidation of NO at an indoor ppb level was evaluated. NO is a common air pollutant mainly discharged from the combustion of fuels and can cause or worsen respiratory diseases and acid rain [57,58]. Fig. 6A shows the removal ratio of NO under the visible-light illumination ($\lambda > 420$ nm). Before illumination, the g-C₃N₄/GO-wrapped sponge adsorbs NO under a flowing NO gas to reach

surface adsorption-desorption equilibrium and the initial concentration of NO is 500 ppb. After turning on the light source, the amount of NO decreased rapidly and achieved the lowest point at ca. 6 min (Fig. 6A). Then the amount of NO increased slowly, which is due to the cover of reaction products (such as NO_2 , NO_3^-) on the active sites [59]. MS has almost no photocatalytic activity, while the max removal ratio of NO is only 2.2% on GO-wrapped sponge. With the increasing amount of $\text{g-C}_3\text{N}_4$, the max removal ratio of NO improves to 4.2%, 12.2%, 34.6%, 44.1%, and 45.9% with the weight ratio of $\text{g-C}_3\text{N}_4$ and GO of 1:1, 3:1, 5:1, 7:1 and 9:1, respectively. It is worth noting that despite the $\text{g-C}_3\text{N}_4$ /GO-wrapped sponge with the $\text{g-C}_3\text{N}_4$ and GO ratio of 9:1 shows the highest photocatalytic performance, its photodegradation efficiency is lower than the sample of 7:1 as shown in Fig. S6A, which is due to the aggregation of excess $\text{g-C}_3\text{N}_4$. Therefore, it does not mean the more the better for the loaded $\text{g-C}_3\text{N}_4$ powder. Importantly, as one kind of product of NO oxidation, NO_2 may lead to bronchitis, reduced immunity, and heart disease, resulting in secondary pollution [60]. Fig. S6B shows the fraction of generated NO_2 . After illumination for 30 min, all the samples reveal a low NO_2 generation fraction below 11%, indicating the favorable selectivity for NO removal. Furthermore, the $\text{g-C}_3\text{N}_4$ /GO-wrapped sponge with the $\text{g-C}_3\text{N}_4$ and GO weight ratio of 7:1 was selected for the photocatalytic recycling test as shown in Fig. 6B. With no treatment before illumination, the removal ratio of NO distinctly decreased within five recycles and finally became steady approximately at 16%, which is mainly attributed to the block of reaction products adsorbed on the active sites of the photocatalyst [59]. After the removal of these adsorbed products through UV illumination for 5 min, the removal ratio of NO on the $\text{g-C}_3\text{N}_4$ /GO-wrapped sponge increased to 29.8% and then stabilized at ca. 28.0% within three recycles. Moreover, oxygen-containing functional groups on the surface of GO plays a positive role in the NO oxidation [35]. However, after the treatment of UV illumination, the oxygen-containing function groups were reduced and the sample becomes black [61], leading to a lower activity than the first run. Interestingly, it is found that the $\text{g-C}_3\text{N}_4$ /GO-wrapped sponge maintains favorable photocatalytic activity under UV-vis light illumination within five consecutive cycles (Fig. 6C), confirming the efficient removal of adsorbed intermediate products under UV light in contrast to visible light.

Notably, the obtained $\text{g-C}_3\text{N}_4$ /GO-wrapped sponge monoliths also possess an outstanding photoreduction activity. CO_2 mainly caused by human activities and burning of fossil fuels has been considered as one of the common greenhouse-effect gases that lead to the global warming [1]. Photoreduction of CO_2 can not only decrease the influence on the climatic change but also produce clean energy such as CO and CH_4 . For this purpose, CO_2 photoreduction test was performed. Fig. 6D shows the generation rate of CO, CH_4 and H_2 over $\text{g-C}_3\text{N}_4$ powder, $\text{g-C}_3\text{N}_4$ -wrapped sponge, $\text{g-C}_3\text{N}_4$ /GO composite and $\text{g-C}_3\text{N}_4$ /GO-wrapped sponge, respectively. Due to the rapid recombination of photogenerated carriers, $\text{g-C}_3\text{N}_4$ powder revealed a very low CO and CH_4 evolution rate of 6.3 and $0.52 \mu\text{mol g}^{-1} \text{h}^{-1}$ and no H_2 production was observed. After the introduction of GO, the interfacial interaction between GO and $\text{g-C}_3\text{N}_4$ remarkably increased the separation of electrons and holes [62], resulting in an obviously enhanced CO, CH_4 and H_2 evolution of 14.6, 0.72 and $0.059 \mu\text{mol g}^{-1} \text{h}^{-1}$ compared with pure $\text{g-C}_3\text{N}_4$. Impressively, the photocatalytic activity was significantly increased after applying MS as framework and a highest CO, CH_4 and H_2 production of 42.9, 4.6 and $1.6 \mu\text{mol g}^{-1} \text{h}^{-1}$ was achieved over $\text{g-C}_3\text{N}_4$ /GO-wrapped sponge, which manifested a remarkable 2.9-, 6.4- and 27.1-folds enhancement of that over $\text{g-C}_3\text{N}_4$ /GO composite and are comparable with noble metal/ $\text{g-C}_3\text{N}_4$ photocatalyst [63,64]. This enhanced photocatalytic performance can be attributed to the synergistic effect of GO and MS: GO works as a co-catalyst, lowering the overpotential to inhibit the recombination of photogenerated carriers while the 3D network of MS is endowed with high conductivity after the wrapping of GO, further increasing the separation efficiency of charge carriers which was evidenced by the PL analysis. As shown in Fig. S7, the introduction of GO

remarkably decreased the PL intensity and a further diminished PL intensity could be observed for $\text{g-C}_3\text{N}_4$ /GO-wrapped sponge. The order in the degree of PL inhibition could be matched well with photocatalytic activity. Moreover, it is well known that CO_2 contains delocalized π -conjugation which make it connect with GO through strong π - π conjugation [65,66], resulting in an increased concentration of CO_2 on the surface of GO. Despite the enhanced separation efficiency of photogenerated carriers in $\text{g-C}_3\text{N}_4$ /GO composite, a large amount of $\text{g-C}_3\text{N}_4$ powder covered on the surface of GO and hindered the adsorption of CO_2 . For $\text{g-C}_3\text{N}_4$ /GO-wrapped sponge, the porous structure and large surface area of MS make GO efficiently transfer to the skeleton of MS and increase the contact area of CO_2 with GO, leading to the highest photocatalytic conversion of CO_2 . In addition, $\text{g-C}_3\text{N}_4$ /GO-wrapped sponge revealed a selectivity of ca. 87.4% for the generation of CO, which is higher than the reported Cr/ CeO_2 [67], B/ SrTiO_3 [68], Ag/ CdS /RGO [69], and $\text{g-C}_3\text{N}_4$ -based materials [70,71], as shown in Table S1. Our results demonstrate this multifunctional $\text{g-C}_3\text{N}_4$ /GO-wrapped sponge monoliths possess great promising for environmental remediation and clean energy production.

As demonstrated above, the obtained $\text{g-C}_3\text{N}_4$ /GO-wrapped MS possesses both excellent adsorption capacity and outstanding photocatalytic performance. Therefore, an adsorption-degradation process can be realized over $\text{g-C}_3\text{N}_4$ /GO-wrapped MS as shown in Fig. S8. The as-prepared $\text{g-C}_3\text{N}_4$ /GO-wrapped MS first adsorbed MO until adsorption-desorption equilibrium and then photodegraded MO under light illumination, indicating the multifunction of $\text{g-C}_3\text{N}_4$ /GO-wrapped MS.

Based on the above discussion, a possible photocatalytic mechanism is provided in Fig. 7. Generally, there are three main steps for photocatalysis. Firstly, the pollutants or reactants are adsorbed on the surface of photocatalyst. The synergistic effect of GO and MS makes the $\text{g-C}_3\text{N}_4$ /GO-wrapped sponge possess a larger surface area compared with the powder $\text{g-C}_3\text{N}_4$, leading to an excellent adsorption capacity. Secondly, the photocatalyst absorbs light and excites electrons and holes. The black-body property and surface sensitization of GO strength the visible light absorption [38], resulting in a red shift in the UV-vis spectrum, which can increase the photogenerated electrons and holes. Finally, the photogenerated electrons and holes are transferred to the surface to oxidize NO or reduce CO_2 . The high conductivity of GO provides the effective electrons transfer pathway to avoid the recombination of electrons and the uniformly dispersed GO on the skeleton further accelerates the transfer of electron in line with the analysis of PL (Fig. S7). The band structure diagram of $\text{g-C}_3\text{N}_4$ /GO-wrapped

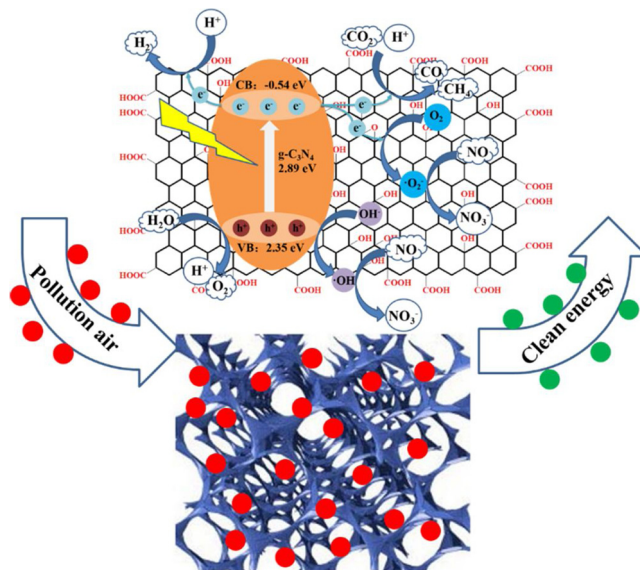
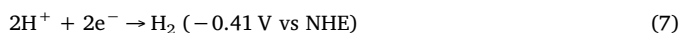
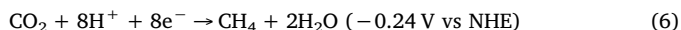
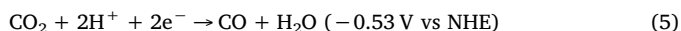
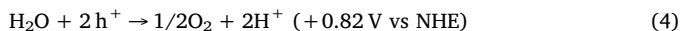


Fig. 7. The proposed photocatalytic mechanism for photooxidation NO and photoreduction CO_2 on $\text{g-C}_3\text{N}_4$ /GO-wrapped sponge.

sponge based on the XPS valence band spectrum (Fig. S9A) and UV–vis spectrum (Fig. 3B) is also shown in Fig. 7. The g-C₃N₄/GO-wrapped sponge possesses relatively positive valence band of 2.35 eV, revealing its favorable oxidation activity [35]. Typically, hydroxyl radical ($\cdot\text{OH}$) (1.99 eV), superoxide radical ($\cdot\text{O}_2$) (−0.28 eV) and photogenerated h^+ are the species for photooxidation while photogenerated e^- is that for photoreduction. Except for the direct oxidation of NO by h^+ , ESR spectra (Fig. S9B) and radical capture experiment (Fig. S8) confirmed that the $\cdot\text{O}_2$ are the main oxidation species for NO removal while for the reduction of CO₂, photogenerated h^+ and e^- react with CO₂ and H₂O through the followed main equations [72]:



Overall, it can be concluded that the synergistic effect between GO and MS enlarged the surface area, enhanced the light absorption and accelerated the separation of photogenerated electrons and holes, resulting in an improved photocatalytic performance.

4. Conclusion

In summary, we reported the successful development of a new-type g-C₃N₄/GO-wrapped sponge monolith prepared through a facile dipping-squeezing method followed by frozen-drying. In this system, g-C₃N₄ photocatalyst is integrated onto MS through the connection of GO. g-C₃N₄ powder is uniformly dispersed on the surface of GO increasing the absorption of light energy and the contact area with the pollution while GO enhances the separation of photogenerated electrons and holes. Moreover, the excellent elasticity of MS makes it easy to recovery and its porous structure ensure that the reaction gas can fast transfer to the catalytic active site. This new-type monolith makes full use of light energy and avoids the intricate recycle operations. Impressively, the obtained g-C₃N₄/GO-wrapped sponge possesses excellent adsorption capacity towards both dyes (10.7 mg g^{−1} for RhB and 69.7 mg g^{−1} for MB) and organic solvents (49.8–133.4 g g^{−1}) as well as recyclability, revealing its potential application in wastewater treatment. Moreover, the g-C₃N₄/GO-wrapped sponge shows outstanding photooxidation of NO with a max removal ratio of 45.9% and photoreduction of CO₂ with CO, CH₄ and H₂ production rate of 42.9, 4.6 and 1.6 μmol g^{−1} h^{−1}, respectively. This multifunctional g-C₃N₄/GO-wrapped sponge photocatalytic system reveals great promising application in both environmental remediation and clean energy production.

Acknowledgements

We gratefully acknowledge financial support from the Sichuan Provincial International Cooperation Project (2017HH0030), the Scientific Research Starting project of SWPU (2014QH0201) and the Innovative Research Team of Sichuan Province (2016TD0011).

Appendix A. Supplementary data

Supplementary material related to this article can be found, in the online version, at doi:<https://doi.org/10.1016/j.apcatb.2018.04.061>.

References

- [1] C. McGlade, P. Ekins, *Nature* 517 (2015) 187–190.
- [2] K. Caldeira, M.E. Wickett, *Nature* 425 (2003) 365.
- [3] M. Schroepe, *Nature* 472 (2011) 152–154.
- [4] A. Fujishima, K. Honda, *Nature* 238 (1972) 37–38.
- [5] N.S. Lewis, D.G. Nocera, *Proc. Natl. Acad. Sci. U.S.A.* 103 (2006) 15729–15735.
- [6] M.R. Hoffmann, S.T. Martin, W.Y. Choi, D.W. Bahnemann, *Chem. Rev.* 95 (1995)

- 69–96.
- [7] L. Yuliati, H. Yoshida, *Chem. Soc. Rev.* 37 (2008) 1592–1602.
- [8] H. Yoshida, L. Zhang, M. Sato, T. Morikawa, T. Kajino, T. Sekito, S. Matsumoto, H. Hirata, *Catal. Today* 251 (2015) 132–139.
- [9] X.C. Wang, K. Maeda, A. Thomas, K. Takanebe, G. Xin, J.M. Carlsson, K. Domen, M. Antonietti, *Nat. Mater.* 8 (2009) 76–80.
- [10] Y. Wang, X.C. Wang, M. Antonietti, *Angew. Chem. Int. Ed.* 51 (2012) 68–89.
- [11] W.J. Ong, L.L. Tan, Y.H. Ng, S.T. Yong, S.P. Chai, *Chem. Rev.* 116 (2016) 7159–7329.
- [12] P.H. Li, F. Wang, S.Q. Wei, X.Y. Li, Y. Zhou, *Phys. Chem. Chem. Phys.* 19 (2017) 4405–4410.
- [13] R. Kuriki, K. Sekizawa, O. Ishitani, K. Maeda, *Angew. Chem. Int. Ed.* 54 (2015) 2406–2409.
- [14] M. Zhou, P.J. Yang, R.S. Yuan, A.M. Asiri, M. Wakeel, X.C. Wang, *ChemSusChem* 10 (2017) 4451–4456.
- [15] X.D. Zhang, X. Xie, H. Wang, J.J. Zhang, B.C. Pan, Y. Xie, *J. Am. Chem. Soc.* 135 (2013) 18–21.
- [16] J. Xu, L.W. Zhang, R. Shi, Y.F. Zhu, *J. Mater. Chem. A* 1 (2013) 14766–14772.
- [17] G. Liu, P. Niu, C.H. Sun, S.C. Smith, Z.G. Chen, G.Q. Lu, H.M. Cheng, *J. Am. Chem. Soc.* 132 (2010) 11642–11648.
- [18] S.C. Yan, Z.S. Li, Z.G. Zou, *Langmuir* 26 (2010) 3894–3901.
- [19] Z. Li, C. Kong, G.X. Lu, *J. Phys. Chem. C* 120 (2016) 56–63.
- [20] L.B. Jiang, X.Z. Yuan, Y. Pan, J. Liang, G.M. Zeng, Z.B. Wu, H. Wang, *Appl. Catal. B: Environ.* 217 (2017) 388–406.
- [21] L.B. Jiang, X.Z. Yuan, G.M. Zeng, X.H. Chen, Z.B. Wu, J. Liang, J. Zhang, H. Wang, H. Wang, *ACS Sustainable Chem. Eng.* 5 (2017) 5831–5841.
- [22] F. Dong, Z.W. Zhao, T. Xiong, Z.L. Ni, W.D. Zhang, Y.J. Sun, W.K. Ho, *ACS Appl. Mater. Interfaces* 5 (2013) 11392–11401.
- [23] C.S. Pan, J. Xu, Y.J. Wang, D. Li, Y.F. Zhu, *Adv. Funct. Mater.* 22 (2012) 1518–1524.
- [24] D.Q. Zeng, W.J. Ong, H.F. Zheng, M.D. Wu, Y.Z. Chen, D.L. Peng, M.Y. Han, *J. Mater. Chem. A* 5 (2017) 16171–16178.
- [25] D.Q. Zeng, W.J. Xu, W.J. Ong, J. Xu, H. Ren, Y.Z. Chen, H.F. Zheng, D.L. Peng, *Appl. Catal. B: Environ.* 221 (2018) 47–55.
- [26] Z.M. Pan, Y. Zheng, F.S. Guo, P.P. Niu, X.C. Wang, *ChemSusChem* 10 (2017) 87–90.
- [27] D.Q. Zeng, W.J. Ong, Y.Z. Chen, S.Y. Tee, C.S. Chua, D.L. Peng, M.Y. Han, *Part. Part. Syst. Charact.* 35 (2018) 1870003.
- [28] W.J. Ong, *Front. Mater.* 4 (2017).
- [29] L.B. Jiang, X.Z. Yuan, G.M. Zeng, J. Liang, X.H. Chen, H.B. Yu, H. Wang, Z.B. Wu, J. Zhang, T. Xiong, *Appl. Catal. B: Environ.* 227 (2018) 376–385.
- [30] L.B. Jiang, X.Z. Yuan, G.M. Zeng, J. Liang, Z.B. Wu, H. Wang, *Environ. Sci.: Nano* 5 (2018) 599–615.
- [31] F. Chen, Q. Yang, X.M. Li, G.M. Zeng, D.B. Wang, C.G. Niu, J.W. Zhao, H.X. An, T. Xie, Y.C. Deng, *Appl. Catal. B: Environ.* 200 (2017) 330–342.
- [32] K. Wang, G.K. Zhang, J. Li, Y. Li, X.Y. Wu, *ACS Appl. Mater. Interfaces* 9 (2017) 43704–43715.
- [33] Z. Wan, G.K. Zhang, X.Y. Wu, S. Yin, *Appl. Catal. B: Environ.* 207 (2017) 17–26.
- [34] Z.Y. Lin, J.L. Li, Z.Q. Zheng, L.H. Li, L.L. Yu, C.X. Wang, G.W. Yang, *Adv. Energy Mater.* 6 (2016) 1600510.
- [35] W.C. Wan, S. Yu, F. Dong, Q. Zhang, Y. Zhou, *J. Mater. Chem. A* 4 (2016) 7823–7829.
- [36] B.C. Qiu, M.Y. Xing, J.L. Zhang, *J. Am. Chem. Soc.* 136 (2014) 5852–5855.
- [37] R.Y. Zhang, W.C. Wan, D.W. Li, F. Dong, Y. Zhou, *Chin. J. Catal.* 38 (2017) 313–320.
- [38] Y. Zhou, X.J. Zhang, Q. Zhang, F. Dong, F. Wang, Z. Xiong, *J. Mater. Chem. A* 2 (2014) 16623–16631.
- [39] J.X. Low, J.G. Yu, W.K. Ho, *J. Phys. Chem. Lett.* 6 (2015) 4244–4251.
- [40] W.C. Wan, R.Y. Zhang, M.Z. Ma, Y. Zhou, *J. Mater. Chem. A* 6 (2018) 754–775.
- [41] F. Rechberger, M. Niederberger, *Nanoscale Horiz.* 2 (2017) 6–30.
- [42] F. Rechberger, M. Niederberger, *Mater. Horiz.* 4 (2017) 1115–1121.
- [43] J. Ge, L.A. Shi, Y.C. Wang, H.Y. Zhao, H.B. Yao, Y.B. Zhu, Y. Zhang, H.W. Zhu, H.A. Wu, S.H. Yu, *Nat. Nano.* 12 (2017) 434–440.
- [44] C. Wu, X.Y. Huang, X.F. Wu, R. Qian, P.K. Jiang, *Adv. Mater.* 25 (2013) 5658–5662.
- [45] D.D. Nguyen, N.H. Tai, S.B. Lee, W.S. Kuo, *Energy Environ. Sci.* 5 (2012) 7908–7912.
- [46] Z. Tong, D. Yang, J. Shi, Y. Nan, Y. Sun, Z. Jiang, *ACS Appl. Mater. Interfaces* 7 (2015) 25693–25701.
- [47] J.C. Chen, H. You, L.Q. Xu, T.H. Li, X.Q. Jiang, C.M. Li, *J. Colloid Interface Sci.* 506 (2017) 659–668.
- [48] Q. Su, J. Sun, J.Q. Wang, Z.F. Yang, W.G. Cheng, S.J. Zhang, *Catal. Sci. Technol.* 4 (2014) 1556–1562.
- [49] D.J. Merline, S. Vukusic, A.A. Abdala, *Polym. J.* 45 (2013) 413–419.
- [50] X.L. Yang, F.F. Qian, G.J. Zou, M.L. Li, J.R. Lu, Y.M. Li, M.T. Bao, *Appl. Catal. B: Environ.* 193 (2016) 22–35.
- [51] F. Sordello, G. Zeb, K.W. Hu, P. Calza, C. Minero, T. Szkopek, M. Cerruti, *Nanoscale* 6 (2014) 6710–6719.
- [52] J.Z. Ma, J.T. Zhang, Z.G. Xiong, Y. Yong, X.S. Zhao, *J. Mater. Chem.* 21 (2011) 3350–3352.
- [53] R.Y. Zhang, W.C. Wan, L.J. Qiu, Y.H. Wang, Y. Zhou, *Appl. Surf. Sci.* 419 (2017) 342–347.
- [54] F. Chen, Q. Yang, S. Wang, F.B. Yao, J. Sun, Y.L. Wang, C. Zhang, X.M. Li, C.G. Niu, D.B. Wang, G.M. Zeng, *Appl. Catal. B: Environ.* 209 (2017) 493–505.
- [55] L.B. Jiang, X.Z. Yuan, G.M. Zeng, Z.B. Wu, J. Liang, X.H. Chen, L.J. Leng, H. Wang, H. Wang, *Appl. Catal. B: Environ.* 221 (2018) 715–725.
- [56] D. Kim, D.W. Kim, O. Buyukcakir, M.K. Kim, K. Polychronopoulou, A. Coskun, *Adv. Funct. Mater.* 27 (2017) 1700706.

- [57] R.A. Perry, D.L. Siebers, *Nature* 324 (1986) 657–658.
- [58] J.A. Logan, *J. Geophys. Res.* 88 (1983) 10785–10807.
- [59] Y. Liu, S. Yu, Z.Y. Zhao, F. Dong, X.A. Dong, Y. Zhou, *J. Phys. Chem. C* 121 (2017) 12168–12177.
- [60] D.H. Zhang, Z.Q. Liu, C. Li, T. Tang, X.L. Liu, S. Han, B. Lei, C.W. Zhou, *Nano Lett.* 4 (2004) 1919–1924.
- [61] R.Y.N. Gengler, D.S. Badali, D.F. Zhang, K. Dimos, K. Spyrou, D. Gournis, R.J.D. Miller, *Nat. Commun.* 4 (2013) 2560.
- [62] W.J. Ong, L.L. Tan, S.P. Chai, S.T. Yong, A.R. Mohamed, *Nano Energy* 13 (2015) 757–770.
- [63] Y. He, L. Zhang, B. Teng, M. Fan, *Environ. Sci. Technol.* 49 (2015) 649–656.
- [64] W.J. Ong, L.L. Tan, S.P. Chai, S.T. Yong, *Dalton Trans.* 44 (2015) 1249–1257.
- [65] J.G. Yu, J. Jin, B. Cheng, M. Jaroniec, *J. Mater. Chem. A* 2 (2014) 3407–3416.
- [66] W.J. Ong, L.L. Tan, S.P. Chai, S.T. Yong, *Chem. Commun.* 51 (2015) 858–861.
- [67] Y.G. Wang, X. Bai, F. Wang, S.F. Kang, C.C. Yin, X. Li, *J. Hazard. Mater.* (2017), <http://dx.doi.org/10.1016/j.jhazmat.2017.1010.1007> (in press).
- [68] J.J. Shan, F. Raziq, M. Humayun, W. Zhou, Y. Qu, G.F. Wang, Y.D. Li, *Appl. Catal. B: Environ.* 219 (2017) 10–17.
- [69] S.Q. Liu, B. Weng, Z.R. Tang, Y.J. Xu, *Nanoscale* 7 (2015) 861–866.
- [70] W.J. Ong, L.K. Putri, Y.C. Tan, L.L. Tan, N. Li, Y.H. Ng, X.M. Wen, S.P. Chai, *Nano Res.* 10 (2017) 1673–1696.
- [71] S. Zhou, Y. Liu, J.M. Li, Y.J. Wang, G.Y. Jiang, Z. Zhao, D.X. Wang, A.J. Duan, J. Liu, Y.C. Wei, *Appl. Catal. B: Environ.* 158–159 (2014) 20–29.
- [72] X. Li, J.Q. Wen, J.X. Low, Y.P. Fang, J.G. Yu, *Sci. China Mater.* 57 (2014) 70–100.